PHYSICAL REVIEW D **76,** 096002 (2007)

# Stability of the rotating SU(3) Skyrmion

Satoru Akiyama* and Masahiro Kawabata

*Department of Physics, Faculty of Science and Technology, Tokyo University of Science, 2641, Noda, Chiba 278-8510, Japan*

(Received 21 April 2007; revised manuscript received 5 July 2007; published 2 November 2007)

The profile functions of the SU(3) Skyrme soliton are investigated for the octet, decuplet, and antidecuplet baryons by the mean field approach. In this approach, the profile functions are affected by the spatial rotation, the flavor rotation, and the flavor symmetry breaking. The solitons are stable only in the restricted areas of the parameter space for each multiplet. When the flavor symmetry breaking is large, the area for the antidecuplet is narrow compared to those for the octet and decuplet. The parameters are determined by the baryon mass spectrum, and the deformation of the soliton has sizable effects on the masses.

DOI: 10.1103/PhysRevD.76.096002 PACS numbers: 11.30.Rd, 12.39.Dc, 12.39.Mk

## I. INTRODUCTION

Diakonov, Petrov, and Polyakov [1] made a detailed prediction for the masses and the decay widths of the antidecuplet ($\overline{\mathbf{10}}$) baryons in the framework of the Skyrme soliton (Skyrmion) model [2–4]. Following their work, an experimental discovery of the lightest state of $\overline{\mathbf{10}}$, namely $\Theta^+(1540)$, was reported by the LEPS collaboration [5]. $\Theta^+$ has strangeness $S = +1$ and should contain at least one $\bar{s}$ quark. It is called an exotic baryon or a pentaquark, because the minimal number of the quarks is five from the charge and the strangeness. Although later many experiments confirmed this finding, several experiments did not observe $\Theta^+$. Lists of these published experiments and detailed discussion of their results are presented in Refs. [6,7].

Theoretically, there are many works based on the Skyrme model [8], the diquark models [9], the chiral bag model [10], the MIT bag model [11], the constituent quark model [12], the QCD sum rules [13], and the lattice QCD [14]. These works are reviewed in Ref. [15].

We are interested in the descriptions of the $\overline{\mathbf{10}}$ baryons by the soliton [8,16–18] in the SU(3) Skyrme model [19–23]. Now, there are two major approaches to quantize the soliton. First is the Callan-Klebanov approach [24], in which baryons appear as kaon-SU(2) Skyrmion bound states, and the isospin rotation of the soliton and the fluctuations of the kaon field are quantized. The bound states change according to the baryon states. In particular the Wess-Zumino term acts as a repulsive force on the $S = +1$ states; its strength is strong enough to remove all bound states and all resonances for the standard values of the parameters [25]. However, recently, Itzhaki *et al.* [16] applied this approach to the exotic baryons and found the kaon bound states of $S = +1$ by using a large kaon mass ($\sim 1$ GeV).

Second is the rigid rotator approach (RRA) [3], in which the shape of the soliton is common to all baryon states and the rotation of the soliton in flavor space is quantized. Then, the baryons emerge as the rotational states of a rigid soliton. From early papers [21,22] on the SU(3) Skyrme model, it was pointed out that this approach reproduces not only the octet ($\mathbf{8}$) and decuplet ($\mathbf{10}$) baryons but also the antidecuplet ($\overline{\mathbf{10}}$) baryons as the low lying spectrum. The $\overline{\mathbf{10}}$ baryons have the spin and the parity $J^P = 1/2^+$ in this approach.

However, a limit of the applicability of RRA has been pointed out [26–28] in the SU(2) Skyrme model. The shape of the soliton changes because of the centrifugal force of the rotation, and the large spin of the baryon leads to the instability of the soliton due to the spontaneous emission of the real pion from the soliton. In the SU(3) Skyrme model, the low lying multiplets ($\mathbf{8}$, $\mathbf{10}$, and $\overline{\mathbf{10}}$) seem free from the limit of the applicability of RRA [1] due to their small spins. However, the situation depends on the baryon states. The rotation emerges in the strangeness direction simultaneously and pushes the shape of the soliton out further. In addition, if the shape of the soliton is affected by the strangeness degrees of freedom, it would shrink because of the large meson mass. Therefore, there is a possibility too that the flavor symmetry breaking cancels the deformation caused by the rotation. We consider that this possibility should be investigated particularly.

Furthermore, Itzhaki *et al.* [16] and Cohen [17] pointed out that in a large number of the color ($N_c$) expansion, the mass differences between the $\overline{\mathbf{10}}$ and $\mathbf{8}$ baryons scale as $N_c^0$. This means that RRA for multiplet $\overline{\mathbf{10}}$ is not consistent with the large $N_c$ expansion. Since the above mentioned deformations of the classical soliton are formally subleading effects in the expansion, we are interested in whether the effects could be practically negligible in $\overline{\mathbf{10}}$.

In this paper, we formulate a mean field approach to include the effects of the rotation and the symmetry breaking into the shape of the soliton. In this meaning, we modify RRA. In addition, we study numerically the soliton solutions derived from our approach, and find the input parameters that keep the soliton stable and reproduce the baryon mass spectrum.

*akiyama@ph.noda.tus.ac.jp

 

In Sec. II, the SU(3) Skyrme model and its collective quantization are reviewed, and the mean field approach for the soliton is introduced. In Sec. III, the stability conditions of the soliton solution are explained, and the numerical solutions are displayed. In Sec. IV, the input parameters and the resultant baryon mass spectrum are given. Finally, in Sec. V we summarize the results.

## II. SU(3) SKYRME MODEL

### A. Model and the collective coordinate quantization

The effective action [29] we take here is given by

$$\Gamma = \Gamma_S + \Gamma_{SB} + \Gamma_{WZ}, \tag{1}$$

$$\Gamma_S = \int d^4x \left( \frac{f_\pi^2}{4} \mathrm{Tr} \partial_\mu U \partial^\mu U^\dagger + \frac{1}{32e^2} \mathrm{Tr}[U^\dagger \partial_\mu U, U^\dagger \partial_\nu U]^2 \right), \tag{2}$$

$$\Gamma_{SB} = \int d^4x \left\{ \frac{f_\pi^2}{8}(m_\pi^2 + m_\eta^2) \mathrm{Tr}(U + U^\dagger - 2) + \frac{f_\pi^2}{2\sqrt{3}}(m_\pi^2 - m_K^2) \mathrm{Tr}\lambda_8 (U + U^\dagger) \right\}, \tag{3}$$

$$\Gamma_{WZ} = \frac{iN_c}{240\pi^2} \int_{D_5} \mathrm{Tr}(dUU^\dagger)^5, \tag{4}$$

where $f_\pi$ is the pion decay constant, $e$ is the Skyrme parameter, $U(x)$ is the SU(3) unitary matrix representing the pseudoscalar mesons $(\pi, K, \eta)$, $m_{\pi,K,\eta}$ are the masses of $(\pi, K, \eta)$, $\lambda_8$ is the 8th component of the Gell-Mann matrices $\lambda_\mu$ $(\mu = 1, 2, \ldots, 8)$, and $N_c$ is the number of color degrees of freedom. The Wess-Zumino term $\Gamma_{WZ}$ is given as an integral over the five-dimensional disk $D_5$, the boundary of which is the compactified space-time $S_4$. The symmetry breaking mass term $\Gamma_{SB}$ contains only two masses $m_{\pi,K}$ because of the quadratic sum rule: $m_\pi^2 + 3m_\eta^2 - 4m_K^2 = 0$. In this paper, we choose $(e, f_\pi, m_\pi, m_K)$ as adjustable parameters.

The effective action (1) admits a classical static soliton solution under the hedgehog ansatz embedded in the SU(2) subgroup:

$$U(x) \longrightarrow U_0(\mathbf{r}) = \exp\left[ i \sum_{i=1}^{3} \lambda_i \hat{x}_i F(r) \right], \tag{5}$$

where $r = |\mathbf{r}|$, $\hat{x}_i = x_i/r$, and $F(r)$ is the profile function of the soliton. The baryon number one solution is subjected to the boundary conditions

$$F(0) = \pi, \qquad F(\infty) = 0. \tag{6}$$

We postulate the cranking form [3] of the time dependent meson field:

$$U(x) = A(t) U_0(\mathbf{r}) A^\dagger(t), \tag{7}$$

where $A(t)$ describes the adiabatic collective rotation of the system in SU(3) flavor space. Using the standard method [19–23] to quantize the motion on the SU(3) group manifold, we obtain a dimensionless quantized collective Hamiltonian $\tilde{H}$ and a first class constraint on the 8th generator $R_8$ of $\mathrm{SU_R}(3)$:

$$\tilde{H} = \tilde{M}_0 + \frac{e^4}{2}\left(\frac{1}{\tilde{\alpha}^2} - \frac{1}{\tilde{\beta}^2}\right) C_2(\mathrm{SU_R}(2)) - \frac{e^4}{2\tilde{\beta}^2} R_8^2 + \frac{e^4}{2\tilde{\beta}^2} C_2(\mathrm{SU_R}(3)) + \frac{\tilde{\gamma}}{2}[1 - D_{88}^{(8)}(A)], \tag{8}$$

$$R_8 = -\frac{N_c}{2\sqrt{3}}, \tag{9}$$

where $C_2(\mathrm{SU_R}(3))$ and $C_2(\mathrm{SU_R}(2))$ are the Casimir operators of $\mathrm{SU_R}(3)$ and $\mathrm{SU_R}(2)$, respectively. In addition,

$$D_{88}^{(8)}(A) = \tfrac{1}{2}\mathrm{Tr}(\lambda_8 A^\dagger \lambda_8 A), \tag{10}$$

and

$$\tilde{M}_0 = 4\pi \int d\rho \rho^2 \left[ \frac{1}{2}\left(1 + 2\frac{\sin^2 F}{\rho^2}\right) F'^2 + \frac{\sin^2 F}{\rho^2}\left(1 + \frac{\sin^2 F}{2\rho^2}\right) + \tilde{m}_\pi^2 (1 - \cos F) \right], \tag{11}$$

$$\tilde{\alpha}^2 = \frac{8\pi}{3} \int d\rho \rho^2 \sin^2 F \left( F'^2 + 1 + \frac{\sin^2 F}{\rho^2} \right), \tag{12}$$

$$\tilde{\beta}^2 = 4\pi \int d\rho \rho^2 \sin^2 \frac{F}{2} \left( \frac{F'^2}{4} + 1 + \frac{\sin^2 F}{2\rho^2} \right), \tag{13}$$

$$\tilde{\gamma} = \frac{16\pi}{3}(\tilde{m}_K^2 - \tilde{m}_\pi^2) \int d\rho \rho^2 (1 - \cos F), \tag{14}$$

where $\rho = e f_\pi r$, $\tilde{m}_{\pi,K} = m_{\pi,K}/(e f_\pi)$, and $F' = \frac{dF}{d\rho}$. The Hamiltonian $\tilde{H}$ explicitly depends only on $e$ and $\tilde{m}_{\pi,K}$. The Hamiltonian, the classical soliton mass, and the symmetry breaking with the physical unit (MeV) are given by $H = \frac{f_\pi}{e}\tilde{H}$, $M_0 = \frac{f_\pi}{e}\tilde{M}_0$, and $\gamma = \frac{f_\pi}{e}\tilde{\gamma}$, respectively. The moments of inertia with the physical unit (1/MeV) are given by $\alpha^2 = \tilde{\alpha}^2/(e^3 f_\pi)$ and $\beta^2 = \tilde{\beta}^2/(e^3 f_\pi)$.

The state function of the baryon $B$ is labeled as

$$\Psi_B = \Psi \begin{pmatrix} IY & JY_R \\ I_3 & J_3 \end{pmatrix}, \tag{15}$$

where $(J, J_3)$, $(I, I_3)$, $Y$, and $Y_R$ are the eigenvalues of the spin, the isospin, the hypercharge, and the right hypercharge, respectively. The right hypercharge is given by $Y_R = 1$ due to constraint (9). Equation (15) is obtained by solving the following eigenvalue equation,

$$\tilde{H}\Psi_B = \tilde{E}_B \Psi_B, \tag{16}$$

where $\tilde{E}_B$ is the dimensionless energy eigenvalue of the baryon state $\Psi_B$. To solve this equation, we use the Yabu and Ando method [30], in which $\tilde{E}_B$ is given by

$$\tilde{E}_B = \tilde{M}_0 + \frac{e^4}{2}\left(\frac{1}{\tilde{\alpha}^2} - \frac{1}{\tilde{\beta}^2}\right)J(J+1) - \frac{3e^4}{8\tilde{\beta}^2} + \frac{e^4}{2\tilde{\beta}^2}\mathcal{E}_{SB}. \tag{17}$$

Quantity $\mathcal{E}_{SB}$ is the dimensionless eigenvalue of

$$\left[C_2(\mathrm{SU_R}(3)) + \frac{\tilde{\beta}^2\tilde{\gamma}}{e^4}(1 - D^{(8)}_{88}(A))\right]\Psi_B = \mathcal{E}_{SB}\Psi_B. \tag{18}$$

### B. Mean field approach to the baryon states

To solve the eigenvalue Eq. (16) and obtain the baryon states [3,4,30], one should know about the profile function $F(\rho)$ in Eqs. (11)–(14). Here, we define an equation of motion for $F(\rho)$ as

$$\frac{\delta\tilde{\mathcal{H}}_B}{\delta F(\rho)} = 0, \tag{19}$$

where $\tilde{\mathcal{H}}_B$ is a *classical* Hamiltonian for each baryon $B$. In RRA [3], $\tilde{\mathcal{H}}_B = \tilde{M}_0$, and $F$ is not affected by the rotation and the symmetry breaking at all. Therefore, $F$ is common to all baryons.

In this paper, we adopt the following mean field Hamiltonian [31–33],

$$\tilde{\mathcal{H}}_B = \langle\Psi^{(0)}_B|\tilde{H}|\Psi^{(0)}_B\rangle, \tag{20}$$

where $|\Psi^{(0)}_B\rangle$ is an eigenstate of $\tilde{H}$ without the SU(3) symmetry breaking ($\tilde{\gamma} = 0$), and the state is represented by the SU(3) $D$ function corresponding to the baryon $B$.

Our classical Hamiltonian $\tilde{\mathcal{H}}_B$ includes the influence of the flavor symmetry breaking of the first order in powers of $(\tilde{m}_K^2 - \tilde{m}_\pi^2)$ and the influence of the rotation of order $1/N_c$ in the large $N_c$ expansion. The specific expression of $\tilde{\mathcal{H}}_B$ is given by

$$\tilde{\mathcal{H}}_B = \tilde{M}_0 + \frac{e^4}{2}(\tilde{\alpha}^2\tilde{\omega}^2 + \tilde{\beta}^2\tilde{\kappa}^2) + \frac{3}{4}q_B\tilde{\gamma}, \tag{21}$$

where

$$\tilde{\omega}^2 = \frac{1}{\tilde{\alpha}^4}J(J+1), \tag{22}$$

$$\tilde{\kappa}^2 = \frac{1}{\tilde{\beta}^4}\left[C_2(\mathrm{SU_R}(3)) - J(J+1) - \frac{3}{4}\right], \tag{23}$$

$$q_B = \tfrac{2}{3}\langle\Psi^{(0)}_B|1 - D^{(8)}_{88}(A)|\Psi^{(0)}_B\rangle. \tag{24}$$

The quantities $\tilde{\omega}$ and $\tilde{\kappa}$ distinguish the multiplets ($\mathbf{8}$, $\mathbf{10}$, $\overline{\mathbf{10}}$), and the values of $J(J+1)$ and $C_2(\mathrm{SU_R}(3)) - J(J+1) - \frac{3}{4}$ are given at Table I. For the states with $J = I$, $\tilde{\omega}$ and $\tilde{\kappa}$ are regarded as the angular frequencies of the rotation in ordinary space and strangeness direction, respectively. The expectation value $q_B$ is a source of the SU(3) symmetry breaking on the profile function and characterizes each baryon state. Table II shows the values of $q_B$ for the individual $\mathbf{8}$, $\mathbf{10}$, and $\overline{\mathbf{10}}$ baryons. Therefore, the profile functions derived from the classical Hamiltonian (21) change the shapes according to the baryon states. Our approach modifies RRA in this meaning.

TABLE I. SU(3) representation $(p, q)$, spin $J$, $J(J+1)$ in Eq. (22), and $C_2(\mathrm{SU_R}(3)) - J(J+1) - \frac{3}{4}$ in Eq. (23) for multiplets $\mathbf{8}$, $\mathbf{10}$, and $\overline{\mathbf{10}}$.

| | $(p, q)$ | $J$ | $J(J+1)$ | $C_2(\mathrm{SU_R}(3)) - J(J+1) - \frac{3}{4}$ |
|---|---|---|---|---|
| $\mathbf{8}$ | (1, 1) | 1/2 | 3/4 | 3/2 |
| $\mathbf{10}$ | (3, 0) | 3/2 | 15/4 | 3/2 |
| $\overline{\mathbf{10}}$ | (0, 3) | 1/2 | 3/4 | 9/2 |

We obtain the equation of motion for $F(\rho)$ from Eqs. (19) and (21):

$$C_{F''}(\rho, F)F'' + C_{(F')^2}(\rho, F)(F')^2 + C_{F'}(\rho, F)F' + C(\rho, F) = 0, \tag{25}$$

where

$$C_{F''}(\rho, F) = 1 + \frac{2\sin^2 F}{\rho^2} - e^4\left(\frac{2}{3}\tilde{\omega}^2\sin^2 F + \frac{1}{4}\tilde{\kappa}^2\sin^2\frac{F}{2}\right), \tag{26}$$

$$C_{(F')^2}(\rho, F) = \frac{\sin 2F}{\rho^2} - e^4\left(\frac{1}{3}\tilde{\omega}^2\sin 2F + \frac{1}{16}\tilde{\kappa}^2\sin F\right), \tag{27}$$

$$C_{F'}(\rho, F) = \left[1 - e^4\left(\frac{2}{3}\tilde{\omega}^2\sin^2 F + \frac{1}{4}\tilde{\kappa}^2\sin^2\frac{F}{2}\right)\right]\frac{2}{\rho}, \tag{28}$$

$$C(\rho, F) = -\left(1 + \frac{\sin^2 F}{\rho^2}\right)\frac{\sin 2F}{\rho^2} - \tilde{m}^2_{\mathrm{eff}}\sin F + \frac{1}{3}e^4\tilde{\omega}^2\left(1 + \frac{2\sin^2 F}{\rho^2}\right)\sin 2F + \frac{1}{4}e^4\tilde{\kappa}^2\left[1 + (1 + 3\cos F)\frac{\sin^2\frac{F}{2}}{\rho^2}\right]\sin F, \tag{29}$$

TABLE II. Expectation value $q_B$ of Eq. (24), where $B \in \mathbf{8}, \mathbf{10}, \overline{\mathbf{10}}$.

| $B \in \mathbf{8}$ | $N$ | $\Lambda$ | $\Sigma$ | $\Xi$ |
|---|---|---|---|---|
| $q_B$ | 7/15 | 9/15 | 11/15 | 12/15 |
| $B \in \mathbf{10}$ | $\Delta$ | $\Sigma^*$ | $\Xi^*$ | $\Omega$ |
| $q_B$ | 7/12 | 8/12 | 9/12 | 10/12 |
| $B \in \overline{\mathbf{10}}$ | $\Theta^+$ | $N^*_{\overline{10}}$ | $\Sigma^*_{\overline{10}}$ | $\Xi^*_{\overline{10}}$ |
| $q_B$ | 6/12 | 7/12 | 8/12 | 9/12 |

and $\tilde{m}_{\rm eff}$ is an effective meson mass given by

$$\tilde{m}^2_{\rm eff} = \tilde{m}^2_\pi(1 - q_B) + \tilde{m}^2_K q_B. \tag{30}$$

Coupled equations (12), (13), (22), (23), and (25) are self-consistently solved under the boundary conditions (6). Then, independent parameters are $(e, \tilde{m}_{\rm eff})$ only. Therefore the effect of the flavor symmetry breaking on the profile function is expressed by $\tilde{m}_{\rm eff}$. In RRA, $\tilde{m}_{\rm eff} = m_{\rm eff}/(ef_\pi) = m_\pi/(ef_\pi) \ll 1$. In our approach, the effective mass can take a value $\sim\tilde{m}_K$ according to $q_B$. This fact is important. If we estimate that $e = 3.87$, $f_\pi = 44.5$ MeV, and $m_K = 495$ MeV [30], a large effective mass $\tilde{m}_{\rm eff} \sim 2.8$ is obtained. Therefore, we can expect a qualitatively different behavior of the soliton solution in our approach.

## III. SOLITON SOLUTION IN THE MEAN FIELD APPROACH

Our next task is to perform the self-consistent procedure in Sec. II B. The procedure is faced with two kinds of complexity: the instability of the soliton solution and the dependence of the soliton solution on the multiplets. The instability results from Eqs. (6) and (25). The dependence on the multiplet is brought into the calculation by Eqs. (22) and (23). Therefore, we discuss these problems separately in the following sections.

### A. Instability of the soliton solution

To investigate the instability of the soliton solution, we treat $(e^4\tilde{\omega}^2, e^4\tilde{\kappa}^2, \tilde{m}^2_{\rm eff})$ as input parameters in this subsection and the next one. The parameter space is designated as $\mathcal{M}$.

The stable soliton solutions of Eq. (25) are obtained only in a restricted area of $\mathcal{M}$. The restriction has two origins. One is a behavior of the profile function $F$ at $\rho \sim \infty$ due to the centrifugal force of the rotation [26–28]:

$$F \sim \frac{A}{\rho^2}(1 + \mu\rho)e^{-\mu\rho}, \tag{31}$$

$$\mu = \sqrt{\tilde{m}^2_{\rm eff} - e^4(\tfrac{2}{3}\tilde{\omega}^2 + \tfrac{1}{4}\tilde{\kappa}^2)}. \tag{32}$$

Here the rotation pushes $F$ out of the center of the soliton. For the stable soliton solution, the following condition should be satisfied:

$$\tilde{m}^2_{\rm eff} - e^4(\tfrac{2}{3}\tilde{\omega}^2 + \tfrac{1}{4}\tilde{\kappa}^2) \geq 0. \tag{33}$$

Therefore, the rotating SU(3) Skyrmion with $\tilde{m}_{\rm eff} = 0$ is unstable. That is analogous to the result of the rotating SU(2) Skyrmion in the chiral limit [26]. The rotating SU(3) Skyrmion, however, can exist in a limit $(\tilde{m}_\pi = 0, \tilde{m}_K \neq 0)$, because $\tilde{m}^2_{\rm eff} > 0$ from Eq. (30) and Table II.

Another origin of the restriction on $\mathcal{M}$ is a behavior of the coefficient function of $F''$ in Eq. (25). We have the second condition for the stable soliton solution satisfying the boundary conditions (6):

$$C_{F''}(\rho, F(\rho)) > 0. \tag{34}$$

For verification of this condition, we define a curve $F^*$ in the $(\rho, F)$ plane by

$$C_{F''}(\rho, F^*) = 0. \tag{35}$$

Function $F^*$ should not be confused with the profile function $F$. We will show that $F$ satisfying the boundary conditions (6) cannot cross $F^*$ and this requirement is equal to condition (34).

At first, we investigate properties of $F^*$. Since Eq. (35) is a quadratic equation for $\sin^2\frac{F^*}{2}$, it has two formal solutions for fixed $\rho$ and $(e^4\tilde{\omega}^2, e^4\tilde{\kappa}^2)$. These formal solutions, however, do not always support two real number values of $F^*$ in the range $0 \leq F^* \leq \pi$ which has one-to-one correspondence with the range $0 \leq \sin^2\frac{F^*}{2} \leq 1$. If $F^*$ is a real number solution in the range, $\pm F^* + 2n\pi$ ($n$: integer) also are solutions in the other range. Practically, we can restrict the value of $F^*$ to the range $-\pi \leq F^* \leq \pi$, because the boundary conditions (6) ensure that the value of $F$ is in the range. Figure 1 shows the typical forms of $F^*$ for $e^4\tilde{\kappa}^2 < 4$, $e^4\tilde{\kappa}^2 = 4$, and $e^4\tilde{\kappa}^2 > 4$. The form of $F^*$ changes drastically at $e^4\tilde{\kappa}^2 = 4$. In particular, there are the constant solutions $F^* = \pm\pi$ for $e^4\tilde{\kappa}^2 = 4$, and $F^*$ for $e^4\tilde{\kappa}^2 \geq 4$ always reaches $\rho = 0$. Figure 2 shows also the dependence of $F^*$ on $e^4\tilde{\omega}^2$ in the range $0 \leq F^* \leq \pi$. For a larger value of $e^4\tilde{\omega}^2$, $F^*$ becomes closer to the axes $\rho = 0$ and $F^* = 0$.

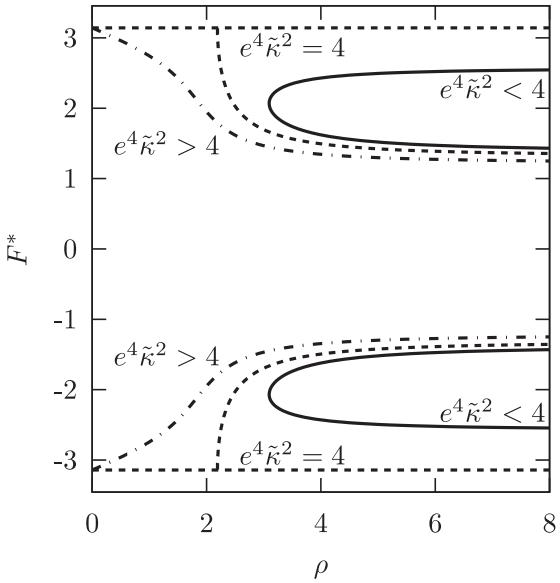


FIG. 1. Typical forms of $F^*$ within $-\pi \leq F^* \leq \pi$. The cases of $e^4\tilde{\kappa}^2 < 4$, $e^4\tilde{\kappa}^2 = 4$, and $e^4\tilde{\kappa}^2 > 4$ are represented by the solid lines, the dashed lines, and the dash-dotted line, respectively. For classification of the lines, we set $e^4\tilde{\omega}^2 \sim 1$.

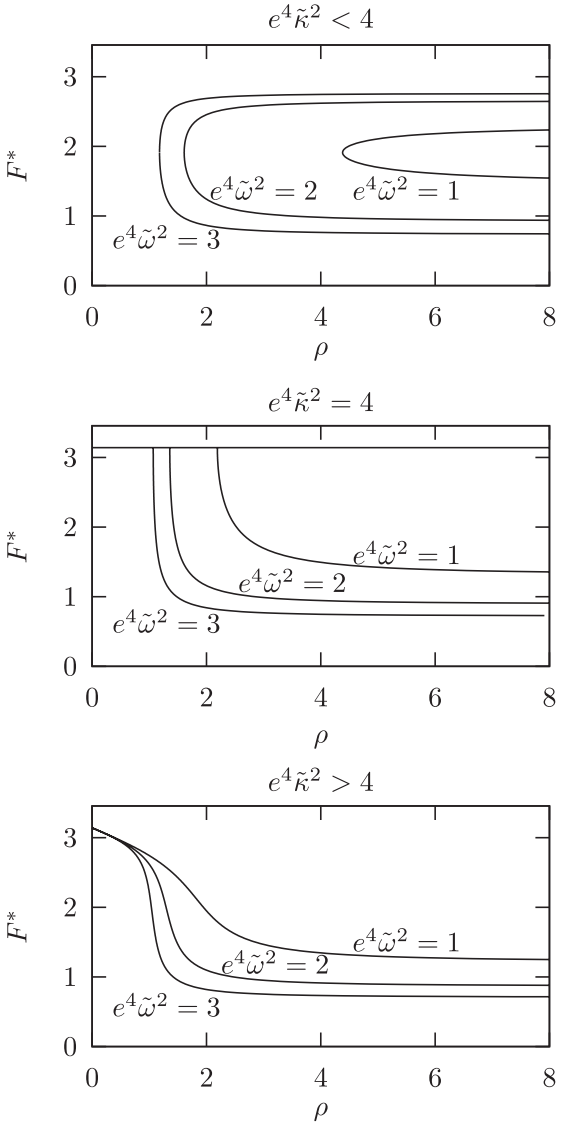


FIG. 2. Typical dependence of $F^*$ on $e^4\tilde{\omega}^2$ in the range $0 \leq F^* \leq \pi$ for $e^4\tilde{\kappa}^2 < 4$, $e^4\tilde{\kappa}^2 = 4$, and $e^4\tilde{\kappa}^2 > 4$. Actual values of $e^4\tilde{\kappa}^2$ in the figures are 3, 4, 5, respectively.

Next, we explain how to verify Eq. (34). If $F$ crosses $F^*$ at some radius $\rho = \rho^*$, Eq. (25) becomes a quadratic equation for $F'(\rho^*)$:

$$C_{(F')^2}(\rho^*, F^*)(F')^2 + C_{F'}(\rho^*, F^*)F' + C(\rho^*, F^*) = 0. \tag{36}$$

Then we can statically calculate the value of the discriminant

$$D^* = C_{F'}(\rho^*, F^*)^2 - 4C_{(F')^2}(\rho^*, F^*)C(\rho^*, F^*). \tag{37}$$

Of course, $D^* < 0$ means that Eq. (36) has no real number solution and $F$ cannot cross $F^*$ at $\rho = \rho^*$ from the beginning. Moreover Eq. (25) does not have the real number solution in a neighborhood of the point, because its discriminant for $F'$:

$$C_{F'}(\rho, F)^2 - 4C_{(F')^2}(\rho, F)C(\rho, F) - 4C_{(F')^2}(\rho, F)C_{F''}(\rho, F)F'' \tag{38}$$

approaches the value of $D^*(<0)$ near $F^*$, and the value of $F'(\rho)$ becomes complex numbers.

For $D^* \geq 0$, the values of $F'(\rho^*)$ are real numbers. However it is analytically unclear whether the values are consistent with the boundary conditions (6). From numerical calculations, we conclude also here that $F$ and $F^*$ cannot cross.

Figures 3 and 4 show the examples. Profile functions $F_i$ ($i = 0, 1, 2, 3$) and $F^*$ for $e^4\tilde{\kappa}^2 < 4$ are plotted in Fig. 3. Each of $F_i$ corresponds to different values of $F'(0)$, namely

$$0 > F_3'(0) > F_2'(0) > F_0'(0) > F_1'(0). \tag{39}$$

Only $F_0$ satisfies the boundary conditions (6). In the cases of $F_{1,2}$, there are breakdowns of Eq. (25), because the profile function approaches the $D^* < 0$ part of $F^*$. Profile function $F_3$ survives but does not satisfy the boundary conditions (6) due to the scattering by the $D^* > 0$ part.

Figure 4 shows $F_i$ ($i = 0, 1, 2, 3$) and $F^*$ for $e^4\tilde{\kappa}^2 > 4$. Also here, only $F_0$ satisfies the boundary conditions (6), and $F_{1,2}$ break because of the same reason as that of the case $e^4\tilde{\kappa}^2 < 4$. Moreover, there is a new situation that $F^*$ divides $F_3$ from the other profiles (e.g. $F_2$). Therefore, $F_2$ is in $C_{F''} > 0$ area and $F_3$ is in $C_{F''} < 0$ area. Although the values of $F_2'(0)$ and $F_3'(0)$ are close, the profile functions $F_2$ and $F_3$ separate with an increase in $\rho$. It seems that there is a repulsion between $F$ and the $D^* > 0$ part of $F^*$. Profile function $F_3$ survives near the $D^* > 0$ part at small $\rho$ but breaks near the $D^* < 0$ part at last.

From these results, we conclude that $F$ satisfying the boundary conditions (6) cannot cross $F^*$. Therefore, $F^*$ divides the $(\rho, F)$ plane into two areas: $C_{F''} > 0$ area and $C_{F''} < 0$ area. Profile function $F(\rho)$ lives in only one area

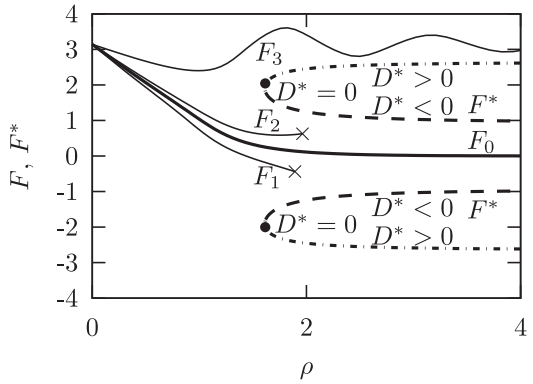


FIG. 3. Profile functions $F_i$ ($i = 0, 1, 2, 3$) and curves $F^*$ for $e^4\tilde{\kappa}^2 < 4$ ($e^4\tilde{\kappa}^2 = 3$, $e^4\tilde{\omega}^2 = 2$, $\tilde{m}_{\text{eff}} = 2$). The solid lines represent $F_i$. The dashed lines indicate $D^* < 0$ parts of $F^*$, the dash-dotted lines $D^* > 0$ parts, and marks "•" represent the points at which $D^* = 0$. Marks "×" represent breakdowns of Eq. (25) at these points.

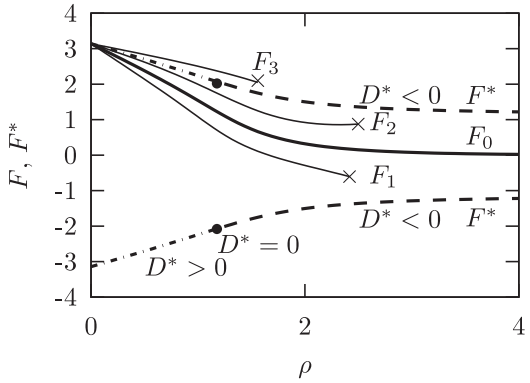


FIG. 4. Profile functions $F_i$ ($i = 0, 1, 2, 3$) and curves $F^*$ for $e^4\tilde{\kappa}^2 > 4$ ($e^4\tilde{\kappa}^2 = 10$, $e^4\tilde{\omega}^2 = 0.5$, $\tilde{m}_{\rm eff} = 1.9$). Meanings of the figure symbols are the same as those of Fig. 3.

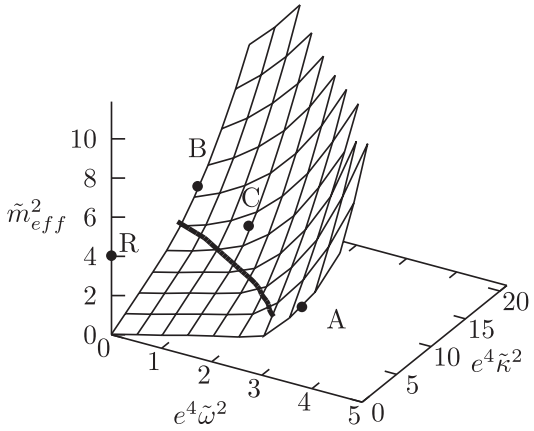


FIG. 5. Critical surface given by Eqs. (6) and (25) in parameter space $\mathcal{M}$. The sizes of the mesh on the surface are $(\Delta e^4\tilde{\omega}^2, \Delta e^4\tilde{\kappa}^2) = (0.5, 2.0)$. The area of the stable soliton is on the upper side of the surface. The solid line on the critical surface indicates the boundary curve ($\tilde{m}_{\rm eff} \sim 1.6$) at which two conditions (33) and (34) change the roles. Point R is placed at (0, 0, 4). Points A, B, and C are placed at (3.5, 0, 4), (0, 12.7, 4) and (1.5, 9, 4), respectively, and are slightly above the surface.

containing the boundary point $(\rho, F) = (\infty, 0)$ of Eq. (6). Since $C_{F''}(\infty, 0) = 1 > 0$ at the boundary point, we obtain condition (34) of the stable soliton solution.

We should choose the value of $F'(0)$ carefully so that $F$ is away from the $D^* < 0$ part of $F^*$. Since $F^*$ approaches the axes $\rho = 0$ and $F^* = 0$ at the larger values of $e^4\tilde{\omega}^2$ and $e^4\tilde{\kappa}^2$ (Figs. 1 and 2), the choice of $F'(0)$ becomes more difficult. This situation improves for the larger value of $\tilde{m}_{\rm eff}$, because $F$ dumps faster according to Eq. (31). Thus, with an increase in $\tilde{m}_{\rm eff}$, the area given by Eq. (34) enlarges with $\tilde{m}_{\rm eff}$ in parameter space $\mathcal{M}$.

### B. Profile function of the stable soliton solution

In this subsection, we discuss several constraints on the parameter space $\mathcal{M}$ and the stable soliton solutions of Eq. (25). At this stage, we have two conditions (33) and (34) for the stable soliton solutions. Condition (33) is explicitly parametrized by $(e^4\tilde{\omega}^2, e^4\tilde{\kappa}^2, \tilde{m}^2_{\rm eff})$, and condition (34) implicitly. Both the conditions define together an area of the stable soliton in $\mathcal{M}$. In Fig. 5, we show a critical surface that separates the areas of the stable solution and the unstable solution in $\mathcal{M}$. The area of the stable soliton is on the upper side of the surface.

Condition (33) defines the critical surface for a small value of $\tilde{m}_{\rm eff}$, and condition (34) does so for a large value of $\tilde{m}_{\rm eff}$. There is a boundary curve, at which these conditions change the roles on the critical surface. The boundary has $\tilde{m}_{\rm eff} \sim 1.6$. We designate the lower (higher) critical surface as $\mathcal{S}_{L(H)}$. $\mathcal{S}_L$ is a plane, because Eq. (33) is a linear equation for $(e^4\tilde{\omega}^2, e^4\tilde{\kappa}^2, \tilde{m}^2_{\rm eff})$. $\mathcal{S}_H$ curves upward steeply.

Here, we illustrate the effects of the rotation and the symmetry breaking with the four points R, A, B, and C depicted in Fig. 5. Point R is placed at $(e^4\tilde{\omega}^2, e^4\tilde{\kappa}^2, \tilde{m}^2_{\rm eff}) = (0, 0, 4)$ in $\mathcal{M}$. Points A, B, and C are placed at (3.5, 0, 4), (0, 12.7, 4), and (1.5, 9, 4), respectively, and they are slightly above the critical surface $\mathcal{S}_H$. Figure 6 shows the profile function, its derivatives, and curve $F^*$ [Eq. (35)] with the parameters corresponding to points R, A, B, and C in $\mathcal{M}$.

Case R corresponds to RRA, because the influence of the rotation is ignored. In Fig. 6, there is a flat part of $F''$ at $\rho \sim 0.5$. It is caused by the large meson mass ($\tilde{m}_{\rm eff} \sim 2$). Although such a large meson mass is unfamiliar in other studies on the profile function, it is legitimate in our approach as noted in Sec. II B. If $\tilde{m}_{\rm eff}$ increases more, the flat part dents downward. However, $F''$ does not cross the zero, and $F'$ monotonically increases.

The profile function with small $\tilde{m}_{\rm eff}$ (the parameters near $\mathcal{S}_L$) is given by spreading the solution of case R according to Eq. (31). Then, the effects of the rotation and the symmetry breaking appear in the single mass parameter $\mu$. If $\tilde{m}_{\rm eff}$ decreases further, $\mu$ becomes a complex number and the soliton becomes unstable because of the emission of the real meson.

In the cases of A, B, and C, there are further characteristic behaviors of the profile functions. Since points A, B, and C are close to $\mathcal{S}_H$ in $\mathcal{M}$, the corresponding profile functions emphasize features of the rotation.

Gradients $|F'(0)|$ in the cases of A, B, and C are small compared with that in the case of R, because the rotation pushes the profile function out of the center of the soliton. Then $F''$ should change largely for $F$ to maintain the asymptotic form (31) with the large $\tilde{m}_{\rm eff}$. Therefore, $F''$ crosses the zero, and the behavior of $F'$ becomes complex.

Case A represents the profile functions deformed by the rapid spatial rotation ($e^4\tilde{\kappa}^2 < 4$ and large $e^4\tilde{\omega}^2$). Curvature $F''$ changes intensely at the intermediate $\rho$ region. This profile function is apparent at this stage, but it is excluded by the self-consistent procedure as noted in the next subsection. Moreover, such a profile function is physically unimportant; point A in Fig. 5 is on the $e^4\tilde{\kappa}^2 = 0$ plane corresponding to the SU(2) Skyrmion and its effective

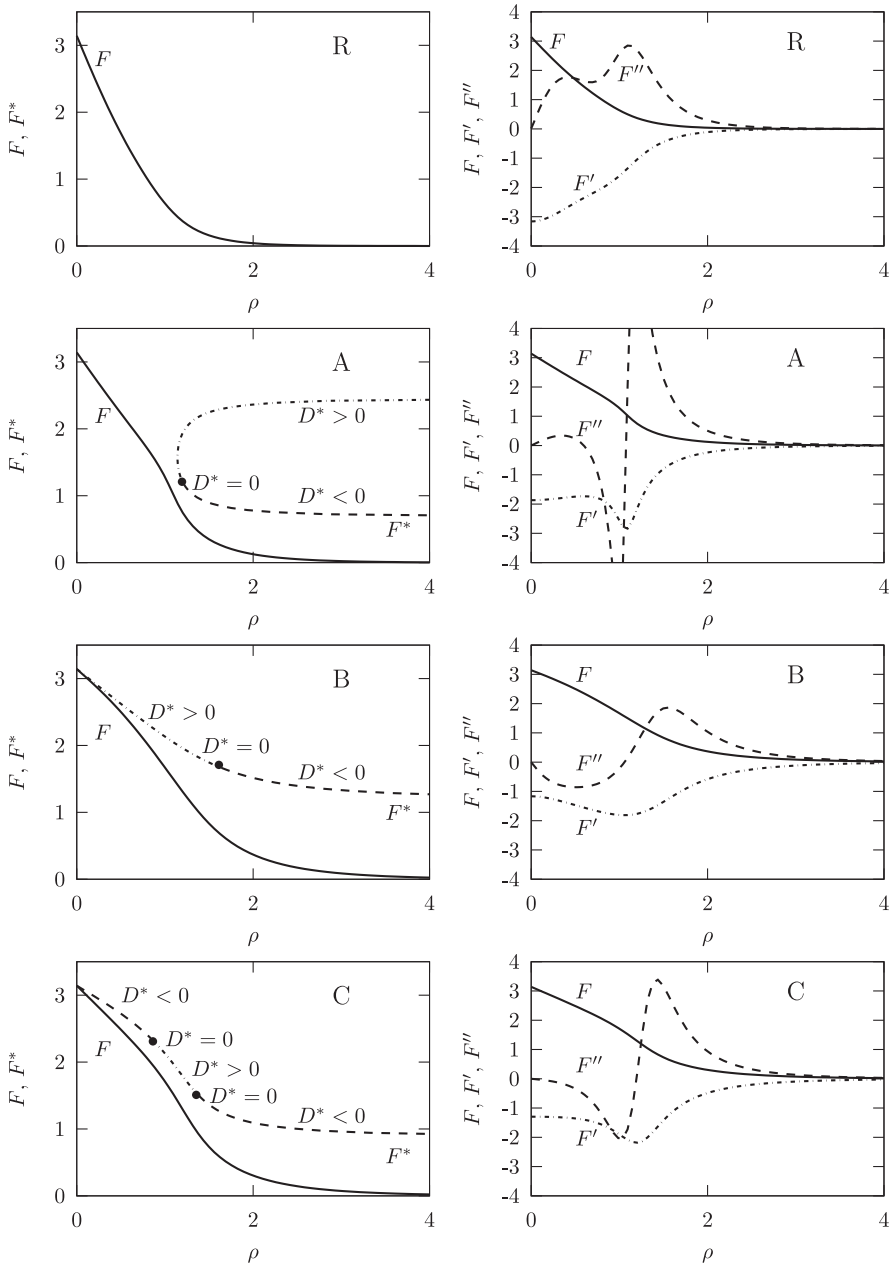


FIG. 6. Left panel: $F$ and $F^*$ for points R, A, B, and C depicted in Fig. 5. Right panel: $F$, $F'$, and $F''$ for the points.

mass is large ($\tilde{m}_{\rm eff} \sim 2$), however, physically $\tilde{m}_{\rm eff} = m_\pi/(ef_\pi) \ll 1$ in this sector.

Case B represents the profile functions affected by the rapid flavor rotation ($e^4\tilde{\kappa}^2 > 4$ and small $e^4\tilde{\omega}^2$). Curvature $F''$ is already negative at $\rho \sim 0$. Since $F^*$ reaches $\rho = 0$, Eq. (34) reduces to

$$1 + 2F'(0)^2 - \frac{e^4\tilde{\kappa}^2}{4} > 0, \tag{40}$$

according to the boundary conditions (6). If $\tilde{m}^2_{\rm eff}$ decreases, $F'(0)^2$ becomes too small and Eq. (40) fails.

Case C represents the profile functions affected by both the spatial and the flavor rotation ($e^4\tilde{\kappa}^2 > 4$ and the medium value of $e^4\tilde{\omega}^2$). Although $F^*$ reaches $\rho = 0$ and Eq. (40) is valid here too, the spatial rotation affects the profile function at $\rho \sim 1$ and $F''$ changes greatly there. This spatial rotation has smaller angular frequency than that of case A. Therefore, the flavor rotation enhances the effect of the spatial rotation.

### C. Self-consistent soliton solution and the dependence of the classical soliton on the multiplets

We are ready to study the self-consistent solution of the coupled equations (12), (13), (22), (23), and (25), and the boundary conditions (6). The independent parameters reduce from ($e^4\tilde{\omega}^2$, $e^4\tilde{\kappa}^2$, $\tilde{m}^2_{\rm eff}$) to ($e$, $\tilde{m}_{\rm eff}$), and the quantities

$(\tilde{\omega}^2, \tilde{\kappa}^2)$ are self-consistently determined for each multiplet **8**, **10**, and $\overline{\mathbf{10}}$. From Table I and Eqs. (22) and (23), one can estimate that

$$\tilde{\omega}^2|_{\mathbf{10}} \sim 5 \times \tilde{\omega}^2|_{\mathbf{8}}, \tag{41a}$$

$$\tilde{\kappa}^2|_{\mathbf{10}} \sim \tilde{\kappa}^2|_{\mathbf{8}} \tag{41b}$$

for **8** and **10**, and

$$\tilde{\omega}^2|_{\overline{\mathbf{10}}} \sim \tilde{\omega}^2|_{\mathbf{8}}, \tag{42a}$$

$$\tilde{\kappa}^2|_{\overline{\mathbf{10}}} \sim 3 \times \tilde{\kappa}^2|_{\mathbf{8}} \tag{42b}$$

for **8** and $\overline{\mathbf{10}}$, and

$$\tilde{\omega}^2|_{\overline{\mathbf{10}}} \sim \tfrac{1}{5} \times \tilde{\omega}^2|_{\mathbf{10}}, \tag{43a}$$

$$\tilde{\kappa}^2|_{\overline{\mathbf{10}}} \sim 3 \times \tilde{\kappa}^2|_{\mathbf{10}} \tag{43b}$$

for **10** and $\overline{\mathbf{10}}$.

Since the number of the independent parameters is two, the self-consistent solutions form surfaces for each multiplet in the parameter space $\mathcal{M}$. The surfaces are limited by the critical surface in Fig. 5. We call the surfaces "self-consistent surfaces" and show these in Fig. 7. In addition, Fig. 8 shows the intersection lines between the critical surface and the self-consistent surfaces on the contour map of the critical surface. The self-consistent surface for **10** is away from the others because of Eqs. (41). Further the surface for $\overline{\mathbf{10}}$ is closer to the $e^4\tilde{\omega}^2 = 0$ plane than the surface for **8** because of Eqs. (42).

These figures are useful for relating the profile functions with multiplets **8**, **10**, and $\overline{\mathbf{10}}$. For example, Fig. 7 shows that the profile functions in case A in Fig. 6 are excluded, because point A is on the $e^4\tilde{\kappa}^2 = 0$ plane in $\mathcal{M}$ and any self-consistent surfaces do not pass through this plane

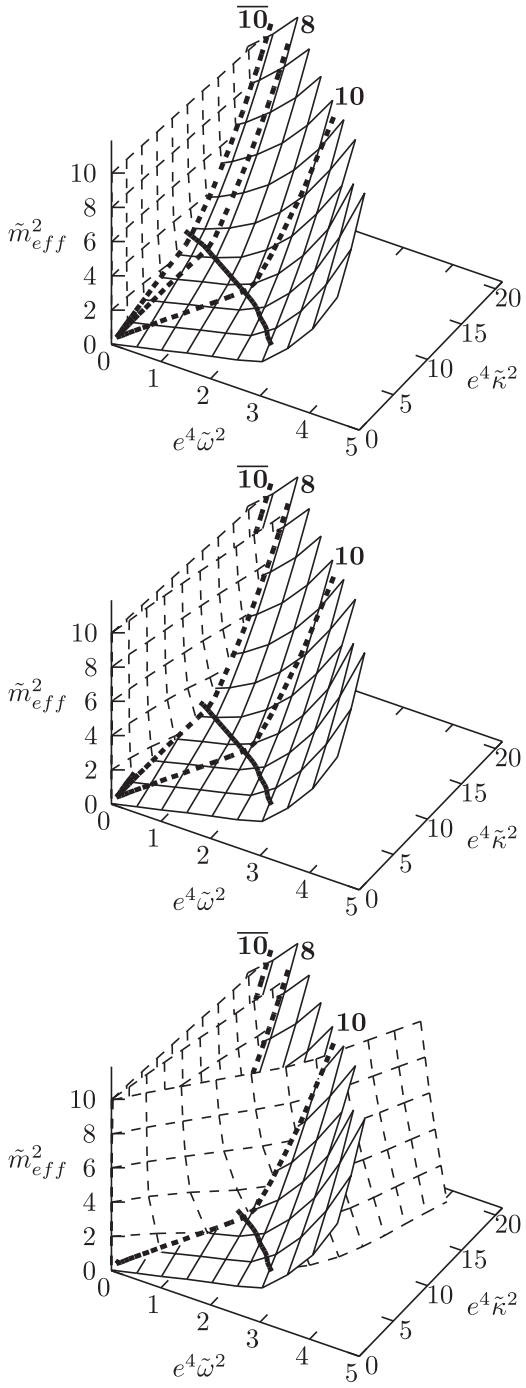


FIG. 7. Self-consistent surfaces for the multiplets **8**, **10**, and $\overline{\mathbf{10}}$ in parameter space $\mathcal{M}$. The dashed lines represent the self-consistent surfaces. Three panels show these surfaces one by one in the order of $\overline{\mathbf{10}}$, **8**, and **10**. The solid lines denote the critical surface in Fig. 5. The dashed lines on the critical surface represent the intersection lines between these two kinds of the surface. The self-consistent surfaces under the critical surface are spurious. They have been shown due to a limit of the ability of our graphic software.

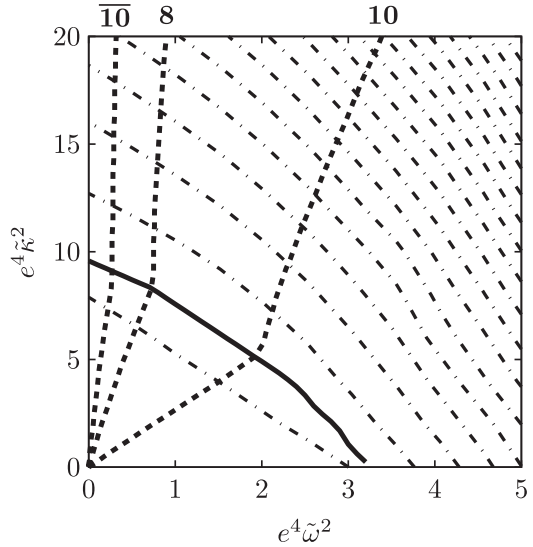


FIG. 8. Intersection lines between the critical surface and the self-consistent surfaces for the multiplets **8**, **10**, and $\overline{\mathbf{10}}$. The dashed lines represent the intersection lines. The dash-dotted lines represent the contour lines of the critical surface with step $\Delta\tilde{m}^2_{\text{eff}} = 2$. The solid line indicates the boundary curve in Fig. 5.

except for the $\tilde{m}_{\rm eff}^2$ axis. However the profile functions in the cases of R, B, and C can be self-consistent solutions.

Figure 8 shows that if the self-consistent solution is evaluated near $\mathcal{S}_H$, always $e^4\tilde{\kappa}^2 > 4$. Then the profile functions of **8** and $\overline{\mathbf{10}}$ are similar to that of case B in Fig. 6, and the profile functions for **10** are similar to that of case C.

Also in parameter space $(e, \tilde{m}_{\rm eff})$, there are curves that separate the area of the stable soliton solutions and the area of the unstable ones in each multiplet. We call the curves ''critical curves'' and show these in Fig. 9. Every curve has an upward ledge at $\tilde{m}_{\rm eff} \sim 1.6$. The left area of the ledge is restricted by Eq. (33), and the right one by Eq. (34). These curves correspond to the intersection lines between the critical surface and the self-consistent surfaces in Fig. 7. One can use this figure to decide whether the adjustable parameters $(e, f_\pi, m_\pi, m_K)$ admit the stable soliton solution through Eq. (30).

The critical curve should reach $(e, \tilde{m}_{\rm eff}) = (0, 0)$ because of Eq. (33). However, it is difficult to decide whether the solution of Eq. (25) is stable for $\tilde{m}_{\rm eff} \sim 0$, because the instability for $\tilde{m}_{\rm eff} \sim 0$ appears at the large radius $\rho \gg 1$. Therefore, we show the curves only for $\tilde{m}_{\rm eff} \geq 0.2$.

For $\tilde{m}_{\rm eff} > 1.6$, the areas of the stable soliton become narrow, because the moments of inertia $(\tilde{\alpha}^2, \tilde{\beta}^2)$ are the decreasing functions of $\tilde{m}_{\rm eff}$ in our approach, and as a result the stability condition (34) with Eqs. (22) and (23) becomes severe for parameter $e$.

From Eqs. (33), (34), (41), and (42), it is reasonable that the critical curve for **8** is higher than those for **10** and $\overline{\mathbf{10}}$ through all values of $\tilde{m}_{\rm eff}$. On the other hand, from Eqs. (33), (34), and (43), it is not clear which critical curve for **10** and $\overline{\mathbf{10}}$ is higher. Indeed, the curves for **10** and $\overline{\mathbf{10}}$ change their relative height according to $\tilde{m}_{\rm eff}$. In particular, the critical curve for $\overline{\mathbf{10}}$ is lower than that for **10** in the area $\tilde{m}_{\rm eff} > 1.6$. It is explained as follows. The self-consistent solutions corresponding to the critical curves are obtained

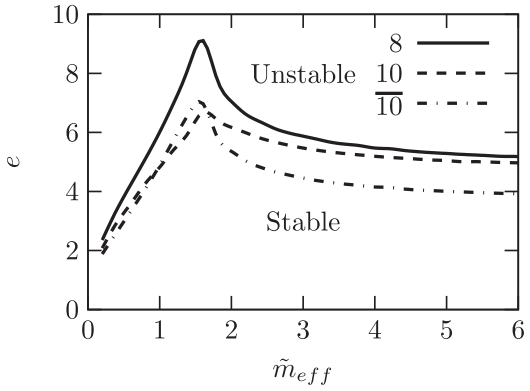


FIG. 9. Critical curves for multiplets **8**, **10**, and $\overline{\mathbf{10}}$ in parameter space $(e, \tilde{m}_{\rm eff})$. These curves separate the areas in which the soliton is stable or unstable. The horizontal axis $\tilde{m}_{\rm eff}$ is different from $m_{\rm eff}/F_\pi = m_{\rm eff}/(2f_\pi)$ of Ref. [28].

near $\mathcal{S}_H$ in Fig. 7, and the solutions have $e^4\tilde{\kappa}^2 > 4$. Therefore, condition (34) reaches $\rho = 0$. For a large effective mass, condition (34) is effective at $\rho \sim 0$ because of Eq. (31) and it reduces to Eq. (40) containing only $\tilde{\kappa}^2$. Since $\tilde{\kappa}^2$ for $\overline{\mathbf{10}}$ is about 3 times larger than that for the other multiplets in Eqs. (42b) and (43b), the area of the stable solitons for $\overline{\mathbf{10}}$ is narrower than those for **8** and **10**.

The terms proportional to $\tilde{\kappa}^2$ in Eqs. (34) and (40) originate from the term $\frac{e^4}{2}\tilde{\beta}^2\tilde{\kappa}^2$ in Eq. (21). This term $\frac{e^4}{2}\tilde{\beta}^2\tilde{\kappa}^2$ is regarded as the coupling between the rotation into the strangeness direction and the amplitude $\sin(F/2)$ in $\tilde{\beta}^2$. The amplitude is the zero mode fluctuation around the hedgehog profile in the flavor symmetry limit [25], and it represents an intrinsic motion on the soliton. If this term becomes large compared with $\tilde{M}_0$ in the mean field Hamiltonian (21), the collective rotation and the intrinsic motion cannot dynamically separate and RRA fails. That is a limit of the applicability of RRA pointed out from a general argument in Ref. [17]. In our approach, the influence of this coupling is dynamically included in the calculation of the profile function through the mean field Hamiltonian (21). Therefore, condition (34) represents a more realistic limit so that the coupling does not destroy the soliton itself.

## IV. BARYON MASS

With the profile function of the stable soliton, the classical soliton mass (11), the moments of inertia (12) and (13), and the symmetry breaking (14) are evaluated. Then the eigenvalue equation (16) can be numerically solved by the Yabu and Ando method, and the baryon masses are obtained. We introduce

$$\Delta E^{\rm err} = \sqrt{\sum_{B\in\mathbf{8},\mathbf{10}} (\Delta E_{BN} - \Delta E_{BN}^{\rm exp})^2}, \tag{44}$$

where $\Delta E_{BN}$ is a difference in the predictive value of the mass between the baryon $B$ and the nucleon $N$, and $\Delta E_{BN}^{\rm exp}$ is its experimental value. An isospin multiplet is represented as a baryon $B$ in this formula, because baryons in an isospin multiplet are described by the same soliton solution. The quantity $\Delta E^{\rm err}$ measures an error of the predicted baryon mass splitting for the multiplets **8** and **10**.

The parameters $(e, \tilde{m}_{\rm eff})$ of the stable solitons are placed below the critical curves in Fig. 9. A parameter set $(e, \tilde{m}_\pi, \tilde{m}_K)$ corresponds to the 12 points in the parameter space $(e, \tilde{m}_{\rm eff})$ according to Eq. (30) and Table II. While the Skyrme parameter $e$ determines the vertical positions of the points, the masses $\tilde{m}_{\pi,K}$ give the horizontal positions and the spreads of the points. We discuss only parameters $(e, \tilde{m}_\pi, \tilde{m}_K)$ which admit the existence of the **8**, **10**, and $\overline{\mathbf{10}}$ baryons. Since $(e, \tilde{m}_\pi, \tilde{m}_K)$ are dimensionless, the energy scale $(f_\pi/e)$ cannot be specified, and the stability of the solitons is not sufficient to determine the values of all parameters $(e, f_\pi, m_\pi, m_K)$. Using the degrees of freedom,

we fit the $N-\Delta$ mass difference or the absolute value of the $N$ mass to its experimental value.

Equation (17) gives the experimental value of the $N-\Delta$ mass difference and the accurate baryon mass splitting (small $\Delta E^{\mathrm{err}}$). The parameter set and the predicted baryon masses are shown as (1) in Tables III and IV, respectively. Here, the value of $f_\pi$, 93 (MeV), is given by hand. A larger value of $f_\pi$ gives a slightly smaller value of $\Delta E^{\mathrm{err}}$, but it leads to extremely larger baryon masses in proportion to $f_\pi$; for example, $\Delta E^{\mathrm{err}} = 74$ (MeV) and $E_N = 5992$ (MeV) for $e = 2.8$, $f_\pi = 186$ (MeV), $m_\pi = 106$ (MeV), and $m_K = 747$ (MeV). Table V shows the dimensionless effective mass ($\tilde{m}_{\mathrm{eff}}$), the classical mass ($M_0$), the moments of inertia ($\alpha^2$, $\beta^2$), and the symmetry breaking ($\gamma$) for parameter set (1). In our approach, these quantities vary according to the baryon states: $\tilde{m}_{\mathrm{eff}}$ characterizes each baryon state, $M_0$ is the increasing function of $\tilde{m}_{\mathrm{eff}}$, and ($\alpha^2$, $\beta^2$, $\gamma$) are the decreasing functions.

However, Eq. (17) cannot give the experimental value of the $N$ mass and the accurate mass splitting simultaneously in our approach. In particular, the values of the baryon masses are large compared with the observed ones. That is a common phenomena in the Skyrme model [30], but the tendency is more severe in our approach. The experimental values of the baryon masses lead to the smaller value of $f_\pi$ which is the energy scale in this model. Therefore the value of the Skyrme parameter should be large for the rotational energy to generate the mass splitting. However, since the Skyrme parameter is restricted by the critical curves for **10** and $\overline{\mathbf{10}}$ in Fig. 9, the magnitude of the mass splitting is not sufficiently large.

There is a more fundamental method [34–37] for the Skyrme model to reproduce the observed baryon masses. In this method, the Casimir energy ($<0$) due to the existence of the soliton is added to the baryon masses. In RRA, the Casimir energy is the quantity of order $N_c^0$, and the value is common to all baryon states. Therefore the addition of this energy does not change the mass splitting, and one can discuss the mass splitting and the values of the masses separately. In our approach, the Casimir energy changes its value according to the baryon states as well as the shape of the soliton and contributes to the mass splitting too. Thus, our self-consistent procedure should include the effect of the Casimir energy to treat the mass splitting and the masses themselves simultaneously. However, that is a complicated task to be examined in detail here, because the simple analytic form of the Casimir energy is not known.

Instead, we adopt a subtraction method [30] to estimate the effect. In this method, the unsubtracted mass formula (17) is replaced by the subtracted one:

TABLE III. Parameter sets. "Exp." denotes the experimental values.

| Set | (1) | (2) | (3) | Exp. |
|---|---|---|---|---|
| $e$ | 3.00 | 3.40 | 6.05 | — |
| $f_\pi$ (MeV) | 93 | 147 | 46 | 93 |
| $m_\pi$ (MeV) | 196 | 0 | 56 | 140 |
| $m_K$ (MeV) | 1042 | 616 | 551 | 496 |

TABLE IV. Baryon mass differences from the nucleon mass for parameter sets (1), (2), and (3). "Exp." denotes the experimental values. $\Delta E^{\mathrm{err}}$ is defined by Eq. (44). Only row of $N$ gives the absolute values of the nucleon mass. Marks "*" denote the input values for the energy scales. All units are (MeV).

| Set | (1) | (2) | (3) | Exp. |
|---|---|---|---|---|
| $\Delta E^{\mathrm{err}}$ | 90 | 104 | 119 | — |
| **8** | | | | |
| $N$ (abs.) | 3618 | 3483 | 939* | 939 |
| $\Lambda$ | 187 | 177 | 154 | 183 |
| $\Sigma$ | 314 | 310 | 270 | 256 |
| $\Xi$ | 396 | 382 | 326 | 379 |
| **10** | | | | |
| $\Delta$ | 293* | 293* | 307 | 293 |
| $\Sigma^*$ | 445 | 435 | 442 | 445 |
| $\Xi^*$ | 570 | 554 | 551 | 595 |
| $\Omega$ | 672 | 654 | 641 | 733 |
| $\overline{\mathbf{10}}$ | | | | |
| $\Theta^+$ | 708 | 483 | 441 | 601? |
| $N^*_{\overline{10}}$ | 888 | 661 | 613 | ? |
| $\Sigma^*_{\overline{10}}$ | 1022 | 800 | 746 | ? |
| $\Xi^*_{\overline{10}}$ | 1059 | 865 | 819 | ? |

TABLE V. Dimensionless effective mass $\tilde{m}_{\mathrm{eff}}$ and parts of the Hamiltonian for the parameter set (1): classical mass $M_0$, moments of inertia ($\alpha^2$, $\beta^2$), and symmetry breaking $\gamma$.

| | $\tilde{m}_{\mathrm{eff}}$ | (MeV) $M_0$ | ($10^{-3}$/MeV) $\alpha^2$ | $\beta^2$ | (MeV) $\gamma$ |
|---|---|---|---|---|---|
| **8** | | | | | |
| $N$ | 2.60 | 2707 | 6.85 | 2.10 | 1628 |
| $\Lambda$ | 2.92 | 2770 | 6.48 | 1.95 | 1393 |
| $\Sigma$ | 3.22 | 2828 | 6.19 | 1.84 | 1226 |
| $\Xi$ | 3.35 | 2855 | 6.07 | 1.79 | 1159 |
| **10** | | | | | |
| $\Delta$ | 2.89 | 2742 | 6.89 | 2.08 | 1531 |
| $\Sigma^*$ | 3.07 | 2779 | 6.69 | 2.00 | 1406 |
| $\Xi^*$ | 3.25 | 2813 | 6.51 | 1.93 | 1302 |
| $\Omega$ | 3.42 | 2845 | 6.36 | 1.87 | 1216 |
| $\overline{\mathbf{10}}$ | | | | | |
| $\Theta^+$ | 2.69 | 2647 | 7.90 | 2.45 | 2087 |
| $N^*_{\overline{10}}$ | 2.89 | 2681 | 7.63 | 2.34 | 1890 |
| $\Sigma^*_{\overline{10}}$ | 3.07 | 2714 | 7.42 | 2.25 | 1732 |
| $\Xi^*_{\overline{10}}$ | 3.25 | 2746 | 7.23 | 2.17 | 1602 |

$$\tilde{E}_B = \tilde{M}_0 + \frac{e^4}{2}\left(\frac{1}{\tilde{\alpha}^2} - \frac{1}{\tilde{\beta}^2}\right)J(J+1) - \frac{3e^4}{8\tilde{\beta}^2} + \frac{e^4}{2\tilde{\beta}^2}(\mathcal{E}_{SB} - \mathcal{E}_0), \quad (45)$$

where the quantity $\mathcal{E}_0$ is the lowest eigenvalue of Eq. (18) corresponding to the vacuumlike state with $(I, J, Y, Y_R) = (0, 0, 0, 0)$. Equation (45) improves the behavior of $\tilde{E}_B$ by removing the vacuum fluctuation energy according to the increase of the symmetry breaking and reproduce the mass splitting accurately [30].

Table IV shows the baryon masses calculated by Eq. (45) with parameter sets (2) and (3) given at Table III. Set (2) fits the $N - \Delta$ mass difference, and set (3) fits the $N$ mass. Both the parameter sets give the accurate mass splitting. In addition, Table VI gives the values of $\tilde{m}_{\rm eff}$, $M_0$, $\alpha^2$, $\beta^2$, and $\gamma$ for set (2), and Table VII gives those for set (3).

The deformation of the soliton reproduces the mass splitting accurately for any parameter set given at Table III, and it has the sizable effects on the **8**, **10**, and $\overline{\mathbf{10}}$ baryons masses as seen from Tables V, VI, and VII. However the mass splitting is caused by the different terms of the Hamiltonian according to the parameters. For example, the contributions of these terms to the $N - \Xi$ mass difference are estimated at the difference in $(M_0, \frac{1}{2}\alpha^2\omega^2, \frac{1}{2}\beta^2\kappa^2, \frac{3}{4}\gamma q_B)$ calculated to $\Xi$ and $N$. In RRA the $N - \Xi$ mass difference is dominated by the symmetry breaking term. However, in our approach, it is distributed as follows: (147, 7, 60, 126) (MeV) for set (1), (51, 11, 72, 254) (MeV) for set (2), and (17, 14, 98, 201) (MeV) for set (3). Therefore the effects of the rotation and the symmetry breaking mix through the deformation of the soliton each other, and the sizes of the effects are large.

TABLE VI. Dimensionless effective mass and parts of the Hamiltonian for the parameter set (2).

| | $\tilde{m}_{\rm eff}$ | (MeV) $M_0$ | $(10^{-3}/\text{MeV})$ $\alpha^2$ | $\beta^2$ | (MeV) $\gamma$ |
|---|---|---|---|---|---|
| **8** | | | | | |
| $N$ | 0.84 | 3200 | 5.71 | 2.08 | 1134 |
| $\Lambda$ | 0.95 | 3221 | 5.33 | 1.91 | 990 |
| $\Sigma$ | 1.05 | 3241 | 5.04 | 1.78 | 886 |
| $\Xi$ | 1.10 | 3251 | 4.92 | 1.73 | 843 |
| **10** | | | | | |
| $\Delta$ | 0.94 | 3199 | 5.88 | 2.15 | 1181 |
| $\Sigma^*$ | 1.00 | 3211 | 5.65 | 2.04 | 1092 |
| $\Xi^*$ | 1.07 | 3222 | 5.46 | 1.96 | 1018 |
| $\Omega$ | 1.12 | 3234 | 5.30 | 1.89 | 955 |
| $\overline{\mathbf{10}}$ | | | | | |
| $\Theta^+$ | 0.87 | 3174 | 7.23 | 2.74 | 1693 |
| $N^*_{\overline{10}}$ | 0.94 | 3180 | 6.88 | 2.58 | 1550 |
| $\Sigma^*_{\overline{10}}$ | 1.00 | 3187 | 6.59 | 2.46 | 1434 |
| $\Xi^*_{\overline{10}}$ | 1.07 | 3194 | 6.35 | 2.35 | 1338 |

TABLE VII. Dimensionless effective mass and parts of the Hamiltonian for the parameter set (3).

| | $\tilde{m}_{\rm eff}$ | (MeV) $M_0$ | $(10^{-3}/\text{MeV})$ $\alpha^2$ | $\beta^2$ | (MeV) $\gamma$ |
|---|---|---|---|---|---|
| **8** | | | | | |
| $N$ | 1.36 | 578 | 4.77 | 1.85 | 917 |
| $\Lambda$ | 1.54 | 584 | 4.4 | 1.67 | 776 |
| $\Sigma$ | 1.70 | 591 | 4.14 | 1.54 | 675 |
| $\Xi$ | 1.77 | 596 | 4.05 | 1.49 | 635 |
| **10** | | | | | |
| $\Delta$ | 1.52 | 606 | 5.31 | 2.05 | 1013 |
| $\Sigma^*$ | 1.63 | 621 | 5.1 | 1.94 | 902 |
| $\Xi^*$ | 1.72 | 640 | 4.97 | 1.84 | 808 |
| $\Omega$ | 1.81 | 660 | 4.88 | 1.76 | 731 |
| $\overline{\mathbf{10}}$ | | | | | |
| $\Theta^+$ | 1.41 | 613 | 6.87 | 2.84 | 1586 |
| $N^*_{\overline{10}}$ | 1.52 | 619 | 6.49 | 2.66 | 1433 |
| $\Sigma^*_{\overline{10}}$ | 1.62 | 627 | 6.20 | 2.52 | 1307 |
| $\Xi^*_{\overline{10}}$ | 1.72 | 640 | 5.98 | 2.41 | 1198 |

If the baryon masses are given by parameter set (3), the **10** and $\overline{\mathbf{10}}$ baryons are affected obviously by the critical curve, because the set corresponds to the points ($e = 6.17$, $\tilde{m}_{\rm eff} = 1.36$–$1.81$) just below the critical curves for **10** and $\overline{\mathbf{10}}$ in Fig. 9. Then, as mentioned in Sec. III C, the profile functions of **8** and $\overline{\mathbf{10}}$ are similar to that of case B in Fig. 6, and the profile functions of **10** are similar to that of case C.

## V. SUMMARY

In this paper, we have investigated the profile function of the SU(3) Skyrmion depending on the octet, decuplet, and antidecuplet baryon states. The equations of motion for the profile function are given by the variation of the mean field Hamiltonian. The Hamiltonian is the expectation value of the collective Hamiltonian operator for the baryon state and depends on the profile function itself through the moments of inertia. Thus, we should solve the equations of motion self-consistently. As the result, the profile function is affected by not only the rotation of the Skyrmion but also the flavor symmetry breaking.

The influence of the symmetry breaking on the profile function is represented by an effective meson mass which varies according to the baryon states. The effective mass in the rigid rotator approach is the pion mass and is usually small. In our approach, the effective mass can take a value about the kaon mass and, the qualitatively different behavior of the soliton solution emerges.

In general, the rotation pushes the profile function out of the center of the soliton, and the symmetry breaking (the effective meson mass) attracts the profile function. For

small effective mass, these effects are represented by the single mass scale in the asymptotic form of the profile function. Then the instability of the soliton appears as the spontaneous emission of the real meson and restricts the parameter space of the self-consistent solutions. That is similar to the result of the SU(2) Skyrmion.

For large effective mass, the influence of the rotation appears in the three cases. First, the rapid spatial rotation leads to the large variation of the curvature ($F''$) of the profile function at the intermediate radius. Second, the rapid flavor rotation leads to the negative value of the curvature at the small radius. Third, the flavor rotation enhances the effect of the spatial rotation and leads to the large variation of the curvature at the intermediate radius. Although the first case is excluded by the self-consistent calculation, the last two cases can be the self-consistent solutions and restrict the parameter space.

The independent parameters of the self-consistent solution are the Skyrme parameter and the effective meson mass. There are areas of the independent parameters allowed for each multiplet. The allowed value of the Skyrme parameter for the octet baryons is the largest for all values of the effective mass, and those for the decuplet and antidecuplet baryons change the relative size according to the effective mass. At the large effective mass, the allowed value of the Skyrme parameter for the antidecuplet baryons is smaller than those for the octet and decuplet baryons.

The baryon masses are evaluated by the unsubtracted mass formula and the subtracted one, respectively. Then, the deformation of the soliton reproduces the baryon mass splitting accurately with both the mass formulas and has the sizable effects on the baryon masses. Therefore the effects of the rotation and the symmetry breaking cannot separate clearly.

The subtracted mass formula can reproduce not only the mass splitting but also the observed masses, though the pion decay constant is too small. Since the formula is inspired by the Casimir effect, the Casimir energy should be investigated for our self-consistent procedure to solve the problem of the small pion decay constant. It remains as a matter to be researched further.

Other physical properties (e.g. magnetic moment, charge radius, etc.) are affected by the deformation. The study in this direction is in progress.


[1] D. I. Diakonov, V. Yu. Petrov, and M. V. Polyakov, Z. Phys. A **359**, 305 (1997).
[2] T. H. R. Skyrme, Proc. R. Soc. A **260**, 127 (1961).
[3] G. Adkins, C. Nappi, and E. Witten, Nucl. Phys. **B228**, 552 (1983).
[4] G. Adkins and C. Nappi, Nucl. Phys. **B233**, 109 (1984).
[5] T. Nakano *et al.* (LEPS Collaboration), Phys. Rev. Lett. **91**, 012002 (2003).
[6] K. H. Hicks, Prog. Part. Nucl. Phys. **55**, 647 (2005).
[7] M. Danilov, arXiv:hep-ex/0509012.
[8] M. Praszalowicz, Phys. Lett. B **575**, 234 (2003).
[9] R. Jaffe and F. Wilczek, Phys. Rev. Lett. **91**, 232003 (2003); M. Karliner and H. J. Lipkin, Phys. Lett. B **575**, 249 (2003).
[10] A. Hosaka, Phys. Lett. B **571**, 55 (2003).
[11] C. E. Carlson, C. D. Carone, H. J. Kwee, and V. Nazaryan, Phys. Lett. B **573**, 101 (2003).
[12] Fl. Stancu and D. O. Riska, Phys. Lett. B **575**, 242 (2003).
[13] S.-L. Zhu, Phys. Rev. Lett. **91**, 232002 (2003); R. D. Matheus *et al.*, Phys. Lett. B **578**, 323 (2004); J. Sugiyama, T. Doi, and M. Oka, Phys. Lett. B **581**, 167 (2004).
[14] F. Csikor, Z. Fodor, S. D. Katz, and T. G. Kovacs, J. High Energy Phys. 11 (2003) 070; S. Sasaki, Phys. Rev. Lett. **93**, 152001 (2004); N. Mathur *et al.*, Phys. Rev. D **70**, 074508 (2004).
[15] M. Oka, Prog. Theor. Phys. **112**, 1 (2004).
[16] N. Itzhaki, I. R. Klebanov, P. Ouyang, and L. Rastelli, Nucl. Phys. **B684**, 264 (2004).
[17] T. D. Cohen, Phys. Lett. B **581**, 175 (2004); Phys. Rev. D **70**, 014011 (2004).
[18] H. Walliser and H. Weigel, Eur. Phys. J. A **26**, 361 (2005).
[19] E. Guadanini, Nucl. Phys. **B236**, 35 (1984).
[20] P. O. Mazur, M. A. Nowak, and M. Praszalowicz, Phys. Lett. B **147**, 137 (1984).
[21] A. Manohar, Nucl. Phys. **B248**, 19 (1984).
[22] M. Chemtob, Nucl. Phys. **B256**, 600 (1985).
[23] S. Jain and S. R. Wadia, Nucl. Phys. **B258**, 713 (1985).
[24] C. G. Callan and I. R. Klevanov, Nucl. Phys. **B262**, 365 (1985).
[25] C. G. Callan, K. Hornbostel, and I. R. Klevanov, Phys. Lett. B **202**, 269 (1988); N. N. Scoccola, Phys. Lett. B **236**, 245 (1990).
[26] M. Bander and F. Hayot, Phys. Rev. D **30**, 1837 (1984).
[27] E. Braaten and J. P. Ralston, Phys. Rev. D **31**, 598 (1985).
[28] R. Rajaraman, H. M. Sommermann, J. Wambach, and H. W. Wyld, Phys. Rev. D **33**, 287 (1986).
[29] M. Praszalowicz, Phys. Lett. B **158**, 264 (1985).
[30] H. Yabu and K. Ando, Nucl. Phys. **B301**, 601 (1988).
[31] S. Akiyama and Y. Futami, Phys. Rev. D **67**, 074030 (2003).
[32] S. Akiyama and Y. Futami, Phys. Rev. D **69**, 014001 (2004).
[33] S. Akiyama and Y. Futami, arXiv:hep-ph/0607326.
[34] B. Moussallam and D. Kalafatis, Phys. Lett. B **272**, 196 (1991).
[35] G. Holzwarth, Phys. Lett. B **291**, 218 (1992).
[36] G. Holzwarth, Nucl. Phys. **A572**, 69 (1994).
[37] Joon-Il Kim and Byung-Yoon Park, Phys. Rev. D **57**, 2853 (1998).